Acta Mech
https://doi.org/10.1007/s00707-019-02607-4

ORIGINAL PAPER

Leonid P. Obrezkov · Marko K. Matikainen · Ajay B. Harish

A finite element for soft tissue deformation based on the absolute nodal coordinate formulation

Received: 31 May 2019 / Revised: 14 November 2019

Abstract This paper introduces an implementation of the absolute nodal coordinate formulation (ANCF) that can be used to model fibrous soft tissue in cases of three-dimensional elasticity. It is validated against results from existing incompressible material models. The numerical results for large deformations based on this new ANCF element are compared to results from analytical and commercial software solutions, and the relevance of the implementation to the modeling of biological tissues is discussed. Also considered is how these results relate to the classical results seen in Treloar's rubber experiments. All the models investigated are considered from both elastic and static points of view. For isotropic cases, neo-Hookean and Mooney–Rivlin models are examined. For the anisotropic case, the Gasser–Ogden–Holzapfel model, including a fiber dispersion variation, is considered. The results produced by the subject ANCF models agreed with results obtained from the commercial software. For the isotropic cases, in fact, the numerical solutions based on the ANCF element were more accurate than those produced by ANSYS.

1 Introduction

Over the last decade, the mechanical behaviors and computational modeling of soft tissues have been under investigation, and these investigations are receiving increased attention in the literature [17]. Cardiovascular diseases remain a significant factor in disability for Western countries and around the world. Despite years of research, illnesses of the heart, tendons, and arteries, and the mechanisms behind them are still not well-understood [10,26]. This can be attributed, firstly, to the extreme complexity of biological systems. Their proper functioning depends on a wide variety of factors [36]. Secondly, their complex shapes make them difficult to model. Moreover, in vitro experiments are complicated, invasive, and could be subject to error [47]. Computer analysis (finite element method modeling, for example) can be useful and can play a vital role in providing insights into biological problems of interest. Rapid increases in computational power are facilitating the simulation of more and more sophisticated problems that are considering the deformations of complex systems, even in dynamic conditions. However, even with new computational methods, general system models are still challenging to describe. Therefore, it makes sense to consider the system in parts. Two of the more important fundamental parts are arteries and tendons. Modeling arteries and tendons has been addressed in some

L. P. Obrezkov · M. K. Matikainen
Lappeenranta University of Technology, Yliopistonkatu 34, 53850 Lappeenranta, Finland
E-mail: Leonid.Obrezkov@lut.fi

M. K. Matikainen
E-mail: Marko.Matikainen@lut.fi

A. B. Harish (✉)
Institute of Continuum Mechanics, Leibniz University Hannover, Appelstr. 11, 30167 Hannover, Germany
E-mail: harish@ikm.uni-hannover.de

Published online: 14 January 2020

earlier works including Holzapfel [21], Horgan and Saccomandi [15], Li [18], Rachev and Greenwald [37]. To describe the deformation of arteries and tendons, they are usually modeled as beams and shells of different cross section. In standard beam elements using an FEA-based approach (for example, Euler–Bernoulli, Timoshenko, and geometrically exact beam theories [25]), cross-sectional deformation is assumed constant. Although typical in traditional finite element analysis, beam elements do not capture cross-sectional deformation and thus lead to inaccurate solutions for rubber-like materials and biological tissues [24]. Therefore, they are not straightforward to implement for materials laws known from general continuum mechanics. Because of this deficiency, it is important to demonstrate the capacity of the absolute nodal coordinate formulation (ANCF) to accurately model soft tissue deformation.

The ANCF was initially developed by Shabana [39] to model large deformations in multibody dynamics problems. Since then, the ANCF has been a subject of continuous active research [12,29]. In recent years, ANCF elements have also been used to model nonlinear problems [14,20] including those subject to locking effects [35]. The key idea behind the ANCF is to employ spatial shape functions together with the position and global slope coordinates (i.e., tangent and curvature vectors) as degrees of freedom. In displacement field approximations of the beam or plate elements, these functions describe the nodal positions and orientations, respectively. It makes it possible to describe the continuum of a beam or plate-type structures from centerline or mid-plane while considering cross-sectional deformation.

Additionally, the use of slope coordinates that are components of the deformation gradient leads to a unique description of the rotation of the ANCF element. Thus, the formulation facilitates the usage of three-dimensional rotations in the total Lagrangian framework without introducing singularity problems. The ANCF element describes deformation using nodal coordinates without bringing in additional degrees of freedom such as rotations.

The ANCF element automatically describes nonlinear effects [8] and relaxes some assumptions used in Euler–Bernoulli, Timoshenko, Reissner, and Mindlin theories [4,25,27]. Furthermore, the formulation leads to a constant mass matrix, which makes it possible to exclude Coriolis inertia and centrifugal forces from the equations of motion, a computational advantage [27,29,40]. This approach has already been used to describe rubber-like materials. Maqueda and Shaba [23] presented general nonlinear constitutive equations of beams based on the ANCF. The work discussed capturing Poisson modes for three different hyperelastic material models. Orzechowski and Frączeks [34] presented ANCF beam elements that were modeled using nonlinear material models such as incompressible neo-Hookean and two-parameter Mooney–Rivlin. Bauchau et al. [1] discussed slow convergence and locking problems in these ANCF beam elements.

Additionally, if the element has some initial distortions or curvatures, it should be modeled with care to exclude initial strain, because the presence of initial strain can influence the final results and lead to a reduction in the accuracy of numerical outputs [36]. While locking effects are an issue, accurate description of geometry is also a primary concern. Both of these issues need detailed treatment and discussion that is beyond the scope of the current work.

Most of the studies devoted to the ANCF are related to the linear theory of elasticity and do not consider material nonlinearities. In this work, the material models considered are hyperelastic—both isotropic and anisotropic. In particular, we consider three different nonlinear constitutive laws in this investigation: neo-Hookean, Mooney–Rivlin two constants and five constants, and Gasser–Ogden–Holzapfel (GOH) [11]. The usability of the above-mentioned material models is studied in the framework of a 3D three-node ANCF beam element (Nachbagauer et al. [31]).

The novelty of this paper is mainly in the application of nonlinear hyperelastic material models for usage with ANCF-based element formulations. Besides, a thorough comparison is provided here to compare the accuracy and computational efficiency of these novel elemental formulations that can be leveraged to model biological systems in real-time. Further, as a part of the investigation, the study also brings out the errors in the Treloar parameters [45,46], for neo-Hookean and Mooney–Rivlin models, generally used for validation in most studies involving soft materials.

2 Absolute nodal coordinate formulation

The idea behind the ANCF is to use global nodal position and gradient vectors to describe the location of nodes and their orientations, respectively. The position vector is defined as $\boldsymbol{r} = \boldsymbol{r}(x, y, z)$ for any particle in the current configuration, and the position of the initial configuration is defined as $\boldsymbol{r}_0$. The connection between any two vectors is

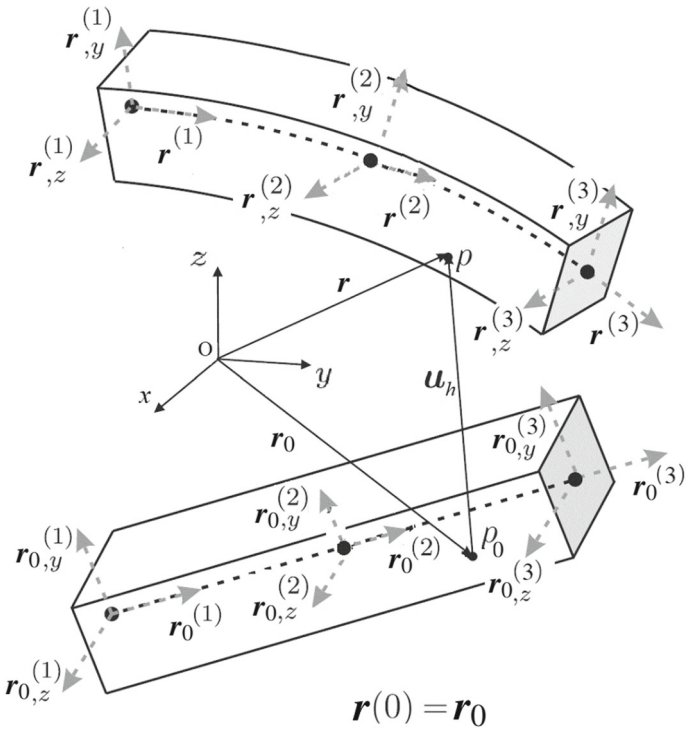

Fig. 1 ANCF three-node element depicting vectors $\boldsymbol{r}$ and $\boldsymbol{r}_0$ related to current and reference configurations, respectively. The nodes are denoted as 1, 2, 3 [7]

$$\boldsymbol{r} = \boldsymbol{r}_0 + \boldsymbol{u}_h$$

where $\boldsymbol{u}_h$ is a displacement vector. Figure 1 provides a visual representation of the position vectors in the Cartesian coordinate system.

In the isoparametric ANCF element, the interpolations of the displacement $\boldsymbol{u}_h(x, y, z)$ and position $\boldsymbol{r}(x, y, z)$ vectors are defined as

$$\boldsymbol{u}_h(x, y, z) = \mathbf{N}_m(x, y, z)\,\boldsymbol{u}, \tag{1}$$

$$\boldsymbol{r}(x, y, z) = \mathbf{N}_m(x, y, z)\,\boldsymbol{q} \tag{2}$$

where $\mathbf{N}_m$ is a shape function matrix, $\boldsymbol{u}$ is a vector of nodal displacements, and $\boldsymbol{q}$ is the vector of the nodal position coordinates. The vector of nodal position coordinates ($\boldsymbol{q}$) is defined for the ith node as

$$\boldsymbol{q}_i = \left[\boldsymbol{r}^{iT}\ \boldsymbol{r}_{,y}^{iT}\ \boldsymbol{r}_{,z}^{iT}\right]^T \tag{3}$$

where the gradients are given as

$$\boldsymbol{r}_{,y}^{i} = \begin{bmatrix} r_{1,y}^{i} \\ r_{2,y}^{i} \\ r_{3,y}^{i} \end{bmatrix} = \frac{\partial \boldsymbol{r}^{i}}{\partial y} \tag{4}$$

and similarly with respect to z. Correspondingly, expanding the vector of nodal coordinates of the element $\boldsymbol{q}$ yields

$$\boldsymbol{q} = \left[\boldsymbol{q}_1^T \quad \boldsymbol{q}_2^T \quad \boldsymbol{q}_3^T\right]^T. \tag{5}$$

To approximate displacement and position fields, the shape function matrix $\mathbf{N}_m$, in Eq. (1), can be formulated with the help of polynomial basis functions for a three-node beam element [30]. The polynomial space of basis functions can be written as

$$\left[1,\ x,\ y,\ z,\ xy,\ xz,\ x^2,\ x^2y,\ x^2z\right]. \tag{6}$$

Since the element under consideration is isoparametric, the shape functions can be expressed by introducing the local coordinate system $\{\xi, \eta, \zeta\}$ with a range for local coordinates of $[-1, 1]$. The local coordinates can be related to the current configuration as follows:

$$\xi = \frac{2x}{l_x},\ \eta = \frac{2y}{l_y},\ \zeta = \frac{2z}{l_z}$$

where the expressions l_x, l_y, and l_z are the physical dimensions of an element. These identities make it possible to apply standard integration procedures such as the Gaussian quadrature rule.

Finally, the expression for the position vector in the current configuration (1) can be written in terms of local binormalized coordinates as

$$\boldsymbol{r} = \mathbf{N}_m\,(\xi, \eta, \zeta)\,\boldsymbol{q} \tag{7}$$

where

$$N_m(\xi, \eta, \zeta) = [N_1\mathbf{I}\ N_2\mathbf{I}\ N_3\mathbf{I}\ \ldots\ N_9\mathbf{I}], \tag{8}$$

and where $\mathbf{I}$ is a 3×3 identity matrix and

$$\begin{aligned}
N_1 &= \frac{1}{2}\xi(\xi - 1)\ N_2 = \frac{1}{4}l_y\xi\eta(\xi - 1),\\
N_3 &= \frac{1}{4}l_z\xi\zeta(\xi - 1)\ N_4 = 1 - \xi^2,\\
N_5 &= \frac{1}{2}l_y\eta(1 - \xi^2)\ N_6 = \frac{1}{2}l_z\zeta(1 - \xi^2),\\
N_7 &= \frac{1}{2}\xi(\xi + 1)\ N_8 = \frac{1}{4}l_y\xi\eta(\xi + 1),\\
N_9 &= \frac{1}{4}l_z\xi\zeta(\xi + 1).
\end{aligned}$$

This element was introduced by Nachbagauer et al. [31]. Referring back to (3) reveals the element to be gradient deficient, i.e., one of the gradient vectors is absent. In this case, the gradient vector with respect to the x coordinate is absent. However, as has been shown in earlier works, elements that include all gradient vectors are more susceptible to shear-locking effects [2,3,5,31]. Moreover, the primary motivation for developing this element is to model tendon and subtendon structures, which are primarily subjected to uniaxial tensile loads. So, for this application, using a gradient-deficient three-node element may be a reasonable choice.

Furthermore, it is essential to highlight that this formulation can be further extended to non-uniform cross-sectional geometries as well. Just as a Joukowsky transformation transforms an airfoil to a circle, the current configuration of any reasonably convex shape can be mapped to a circle/rectangle. This work can be directly extended for irregular cross-sectional geometries by including this transformation and a Jacobian matrix. However, such an implementation is not trivial and merits a detailed accuracy discussion, which is beyond the scope of this work.

3 Equations of motion

The equations of motion can be derived using the Lagrangian of the system based on the principle of virtual work as follows:

$$\delta W_{\text{ext}} + \delta W_{\text{elast}} + \delta W_{\text{inert}} = 0 \tag{9}$$

where W_{ext} is the virtual work by external forces, W_{elast} is the virtual work by elastic forces, and W_{inert} is the virtual work by inertial forces [29]. The variation of virtual work by inertial forces with respect to the nodal coordinates can be written as

$$\delta W_{\text{inert}} = -\ddot{\boldsymbol{q}}^T \int_V \rho \mathbf{N}_m^T \mathbf{N}_m\ \mathrm{d}V \cdot \delta\boldsymbol{q} \tag{10}$$

where ρ is the mass density, and V is the volume of the element in the reference configuration. The expression under the integral is usually called the mass matrix and can be written as

$$M = \int_V \rho \mathbf{N}_m^T \mathbf{N}_m \, \mathrm{d}V. \tag{11}$$

Similarly, the variation of W_{elast} with respect to the nodal coordinates is

$$\delta W_{\text{elast}} = \int_V \mathbf{S} : \delta \mathbf{E} \mathrm{d}V = \int_V \mathbf{S} : \frac{\partial \mathbf{E}}{\partial \boldsymbol{q}} \mathrm{d}V \cdot \delta \boldsymbol{q} \tag{12}$$

where $\mathbf{S}$ is the second Piola–Kirchhoff stress, and $\mathbf{E}$ is the Green–Lagrange strain given as

$$\mathbf{E} = \frac{1}{2}\left(\mathbf{F}^T \cdot \mathbf{F} - \mathbf{I}\right) \tag{13}$$

where $\mathbf{F}$ is the deformation gradient given to be

$$\mathbf{F} = \frac{\partial \boldsymbol{r}}{\partial \boldsymbol{r}_0} = \frac{\partial \boldsymbol{r}}{\partial \xi}\left(\frac{\partial \boldsymbol{r}_0}{\partial \xi}\right)^{-1} = \mathbf{I} + \frac{\partial \boldsymbol{u}_h}{\partial \boldsymbol{r}_0}. \tag{14}$$

Lastly, the variation of external forces has the form

$$\delta W_{\text{ext}} = \int_V \boldsymbol{b}^T \delta \boldsymbol{r} \, \mathrm{d}V = \int_V \boldsymbol{b}^T \mathbf{N}_m \, \mathrm{d}V \cdot \delta \boldsymbol{q} \tag{15}$$

where vector $\boldsymbol{b}$ is the vector of body forces.

4 Material model implementation

The details of the material model and related implementation aspects are discussed in this Section. As in the works of Flory [9], Lu and Pister [22], Ogden [33] and Simo et al. [42], the deformation gradient can be decomposed into dilational (volumetric) and distortion (isochoric) parts.

The determinant of the deformation gradient maps the volumetric changes in the reference and current configurations. Therefore, in this regard, considering continuity, it can be said that

$$J = \det \mathbf{F} > 0. \tag{16}$$

The overall deformation gradient can be decomposed as deviatoric, and the volumetric contributions can be expressed as

$$\mathbf{F} = J^{\frac{1}{3}} \overline{\mathbf{F}} \tag{17}$$

where $\overline{\mathbf{F}}$ represents the deviatoric part of the deformation and follows Eq. (17) with

$$\det \overline{\mathbf{F}} = 1. \tag{18}$$

Correspondingly, the deviatoric parts of the right and left Cauchy–Green deformation tensors are given by

$$\overline{\mathbf{C}} = \overline{\mathbf{F}}^T \cdot \overline{\mathbf{F}}, \quad \overline{\mathbf{B}} = \overline{\mathbf{F}} \cdot \overline{\mathbf{F}}^T. \tag{19}$$

In the isotropic case, all deformations can be defined as functions of the right Cauchy–Green tensor. However, in multibody applications, such as simulating sports injuries in athletes (particularly track and field), accurate modeling of the behavior of tendons and subtendon structures is required. Biomaterials such as tendons demonstrate a directional behavior, because they are made up of fibers oriented in preferred directions. Thus, an anisotropic model is the preferred one to accurately describe their behavior.

In anisotropic materials, like tissues that involve a preferred fiber orientation, orientation must be included in the strain energy formulation. This is achieved as described by the work of Holzapfel and Ogden [17]. Fiber orientation is introduced as a unit vector field $\boldsymbol{a}_0$, which describes the primary direction of the family of

fibers in the reference configuration. Analogously, the vector $\boldsymbol{a} = \overline{\mathbf{F}} \cdot \boldsymbol{a}_0$ denotes the orientation in the current configuration. From continuum mechanics, we can define the square of fiber extension as

$$\lambda_{\boldsymbol{a}_0}^2 = \overline{\mathbf{C}} : \mathbf{A}_0 \tag{20}$$

where $\mathbf{A}_0$ is a structural tensor of order two, with the form

$$\mathbf{A}_0 = \boldsymbol{a}_0 \otimes \boldsymbol{a}_0. \tag{21}$$

Using the structural tensor in (21), the concept developed for one family can be extended to include several families of fibers. Here, the models include up to two families. The second one is denoted as $\boldsymbol{b}_0$ with the corresponding structural tensor being $\mathbf{B}_0$.

In general, the internal energy of the elastic continuum is expressed via the Helmholtz free energy function, which is denoted by Ψ. For a pure isotropic material, the strain energy density function is expressed as a function of the Cauchy–Green deformation tensor only. However, in the presence of anisotropy due to fiber deformation, structural tensors are also considered. A more detailed discussion of this methodology can be found in the works of Gasser et al. [11] and Holzapfel and Gasser [16]. Analogously, the strain energy density for elastic materials reinforced by two families of fibers can be expressed as $\Psi = \Psi(\mathbf{C}, \mathbf{A}_0, \mathbf{B}_0)$.

The additive split of the strain energy density, described earlier in (17), is also commonly known as the F-bar method. It provides a reasonable solution to deal with solids involving incompressibility. Total energy density is decoupled into deviatoric and volumetric parts as follows:

$$\Psi = \overline{\Psi}(\overline{\mathbf{C}}, \mathbf{A}_0, \mathbf{B}_0) + \Psi_{\text{vol}}(J) \tag{22}$$

where $\Psi_{\text{vol}}(J)$ is the volumetric form. In this work, the functional form for the volumetric part is defined as

$$\Psi_{\text{vol}} = \frac{d}{2}(J-1)^2 \tag{23}$$

where d is the penalty coefficient, which is large enough to guarantee incompressibility. A more detailed treatise on various functional forms can be found in the work of Doll and Schweizerhof [6].

The deviatoric part of the strain energy density function can be expressed as a function of the invariants of the Cauchy–Green deformation tensor.

Total strain energy density Ψ for anisotropic materials reinforced by two families of fibers (22) can be written as

$$\Psi = \overline{\Psi}(\overline{I_1}, \overline{I_2}, \overline{I_4}, \ldots, \overline{I_7}) + \Psi_{\text{vol}}(J) \tag{24}$$

where $\overline{I_1}$ and $\overline{I_2}$ are the invariants of $\overline{\mathbf{C}}$ such that

$$\begin{aligned} \overline{I}_1 &= \text{tr}\overline{\mathbf{C}}, \\ \overline{I}_2 &= \frac{1}{2}\left(\text{tr}\,\overline{\mathbf{C}}^2 + \text{tr}^2\overline{\mathbf{C}}\right), \end{aligned} \tag{25}$$

and $\overline{I_4}, \ldots, \overline{I_7}$ are the invariants based on $\overline{\mathbf{C}}$ and tensors $\mathbf{A}_0$ or $\mathbf{B}_0$ [17] such that

$$\begin{aligned} \overline{I}_4 &= \overline{\mathbf{C}} : \mathbf{A}_0, \quad & \overline{I}_5 &= \overline{\mathbf{C}}^2 : \mathbf{A}_0, \\ \overline{I}_6 &= \overline{\mathbf{C}} : \mathbf{B}_0, \quad & \overline{I}_7 &= \overline{\mathbf{C}}^2 : \mathbf{B}_0. \end{aligned} \tag{26}$$

The total second Piola–Kirchhoff stress is known to be

$$\mathbf{S} = 2\frac{\partial \Psi}{\partial \mathbf{C}} = 2\frac{\partial \Psi}{\partial \overline{\mathbf{C}}} : \frac{\partial \overline{\mathbf{C}}}{\partial \mathbf{C}}. \tag{27}$$

Using the form of strain energy density described in (24), this can be expressed as follows:

$$\frac{\partial \overline{\Psi}}{\partial \overline{\mathbf{C}}} = \sum_k \frac{\partial \overline{\Psi}}{\partial \overline{I}_k} \frac{\partial \overline{I}_k}{\partial \overline{\mathbf{C}}}, \tag{28}$$

or in other words

$$\begin{aligned}\mathbf{S} &= 2\frac{\partial\overline{\Psi}}{\partial\overline{\mathbf{C}}}\frac{\partial\overline{\mathbf{C}}}{\partial\mathbf{C}} + 2\frac{\partial\Psi_{\text{vol}}}{\partial J}\frac{\partial J}{\partial\mathbf{C}} \\ &= 2\left(\sum_k \frac{\partial\overline{\Psi}}{\partial\overline{I}_k}\frac{\partial\overline{I}_k}{\partial\overline{\mathbf{C}}}\right)\frac{\partial\overline{\mathbf{C}}}{\partial\mathbf{C}} + \frac{\partial\Psi_{\text{vol}}}{\partial J}J\mathbf{C}^{-1}.\end{aligned} \tag{29}$$

Because

$$\begin{aligned} J^2 = \det\mathbf{C} \Rightarrow \frac{\partial J^2}{\partial\mathbf{C}} &= \frac{\partial(\det\mathbf{C})}{\partial\mathbf{C}}, \\ \frac{\partial(\det\mathbf{C})}{\partial\mathbf{C}} &= (\det\mathbf{C})\,\mathbf{C}^{-1} = J^2\mathbf{C}^{-1}, \\ \frac{\partial J^2}{\partial\mathbf{C}} &= \frac{\partial J^2}{\partial J}\frac{\partial J}{\partial\mathbf{C}} = 2J\frac{\partial J}{\partial\mathbf{C}}, \\ \Rightarrow \frac{\partial J}{\partial\mathbf{C}} &= \frac{1}{2}J\mathbf{C}^{-1}, \\ \Rightarrow 2\frac{\partial\Psi_{\text{vol}}}{\partial J}\frac{\partial J}{\partial\mathbf{C}} = 2\frac{\partial\Psi_{\text{vol}}}{\partial J}\left(\frac{1}{2}J\mathbf{C}^{-1}\right) &= \frac{\partial\Psi_{\text{vol}}}{\partial J}J\mathbf{C}^{-1}, \end{aligned} \tag{30}$$

and substituting for the deviatoric and volumetric parts of the energy, from the work of Weiss et al. [48], the Piola–Kirchhoff stress can be expressed as

$$\mathbf{S} = pJ\mathbf{C}^{-1} + 2J^{-\frac{2}{3}}\left[\frac{\partial\overline{\Psi}}{\partial\overline{\mathbf{C}}} - \frac{1}{3}\left(\frac{\partial\overline{\Psi}}{\partial\overline{\mathbf{C}}} : \overline{\mathbf{C}}\right)\overline{\mathbf{C}}^{-1}\right] \tag{31}$$

where p has the form

$$p = \frac{\partial\Psi_{\text{vol}}(J)}{\partial J}. \tag{32}$$

The derivatives of invariants with respect to the Cauchy–Green deformation tensor are well known [16] and can be written as follows:

$$\begin{aligned} &\frac{\partial\overline{I_1}}{\partial\overline{\mathbf{C}}} = \mathbf{I}, \quad \frac{\partial\overline{I_2}}{\partial\overline{\mathbf{C}}} = \overline{I_1}\mathbf{I} - \overline{\mathbf{C}}, \quad \frac{\partial\overline{I_4}}{\partial\overline{\mathbf{C}}} = \mathbf{A}_0, \\ &\frac{\partial\overline{I_6}}{\partial\overline{\mathbf{C}}} = \mathbf{B}_0 \quad \frac{\partial\overline{I_5}}{\partial\overline{\mathbf{C}}} = \boldsymbol{a}_0 \otimes \overline{\mathbf{C}}\boldsymbol{a}_0, \quad \frac{\partial\overline{I_7}}{\partial\overline{\mathbf{C}}} = \boldsymbol{b}_0 \otimes \overline{\mathbf{C}}\boldsymbol{b}_0. \end{aligned} \tag{33}$$

Although the models assume a single-fiber orientation for all fibers, this is not the reality. Human tissue fibers are dispersed around the assumed fiber orientation, introduced here through $\boldsymbol{a}_0$ and $\boldsymbol{b}_0$. To account for this dispersion, "The κ model" was proposed [11,17]. In the κ model, the dispersion of the fibers is accounted for via the κ parameter and associated with the invariant $I_4^* = \kappa I_1 + (1-3\kappa)I_4$. According to the literature, [11,17], the range of κ values is [0, 0.333]. The lower limit of the range corresponds to zero dispersion, that is, when all fibers are oriented in the same direction. $\kappa = \frac{1}{3}$ corresponds to full dispersion, which correlates with the isotropic model in which the fiber direction, i.e., angles $\boldsymbol{a}_0$, do not affect results. This work also discusses the influence of the parameter on the overall response of anisotropic samples.

5 Material models under consideration

In this Section, the material models used in this investigation are discussed, and the expressions for the deviatoric parts of the strain energy densities of the material models under consideration are given. The volumetric part of the strain energy density term is the same for all models as given in (23). The corresponding volumetric part of the second Piola–Kirchhoff stress is given as

$$\mathbf{S}_{\text{vol}} = d\,(J-1)\,J\mathbf{C}^{-1} \tag{34}$$

The first model considered is the neo-Hookean model. The earliest work that uses this model in conjunction with ANCF elements is the work of Orzechowski and Frączeks [34]. The deviatoric part of the neo-Hookean material model can be given as

$$\overline{\Psi} = c_{10}\left(\overline{I_1} - 3\right), \tag{35}$$

and the corresponding deviatoric part of the second Piola–Kirchhoff stress can be obtained using the expressions (35) and (31) as

$$\overline{\mathbf{S}} = 2c_{10}J^{-\frac{2}{3}}\left[\mathbf{I} - \frac{1}{3}\overline{I}_1\overline{\mathbf{C}}^{-1}\right]. \tag{36}$$

The second type of hyperelastic material models explored for the application of ANCF-type elements are the two- and five-parameter Mooney–Rivlin models [28,38]. The deviatoric part of the strain energy, for the two-parameter Mooney–Rivlin model, is

$$\overline{\Psi} = c_{10}\left(\overline{I_1} - 3\right) + c_{01}\left(\overline{I_2} - 3\right), \tag{37}$$

and the corresponding deviatoric part of the second Piola–Kirchhoff stress is

$$\overline{\mathbf{S}} = 2J^{-\frac{2}{3}}\left[c_{10}\mathbf{I} + c_{01}\left(\overline{I_1}\mathbf{I} - \overline{\mathbf{C}}\right) - \frac{1}{3}\left(c_{10}\overline{I_1} + c_{01}\left(\overline{I_1}^2 - \overline{\mathbf{C}} : \overline{\mathbf{C}}\right)\right)\overline{\mathbf{C}}^{-1}\right]. \tag{38}$$

Analogously, the deviatoric part of the strain energy density for the five-parameter Mooney–Rivlin material is

$$\begin{aligned}\overline{\Psi} = {} & c_{10}\left(\overline{I_1} - 3\right) + c_{01}\left(\overline{I_2} - 3\right) \\ & + c_{20}\left(\overline{I_1} - 3\right)^2 + c_{11}\left(\overline{I_1} - 3\right)\left(\overline{I_2} - 3\right) + c_{02}\left(\overline{I_2} - 3\right)^2.\end{aligned} \tag{39}$$

The next material model under consideration is the anisotropic GOH model [11]. For our purposes, several variations were considered. The first is the sample reinforced by one family of fibers with $\kappa = 0$. This implies that there is no dispersion of fibers or that all of them are oriented along the mean direction. The deviatoric part of the strain energy density is

$$\overline{\Psi} = c_{10}\left(\overline{I_1} - 3\right) + \frac{c_1}{2c_2}\left(e^{c_2(\overline{I_4}-1)} - 1\right), \tag{40}$$

and the corresponding deviatoric part of the second Piola–Kirchhoff stress tensor is

$$\begin{aligned}\overline{\mathbf{S}} = {} & 2J^{-\frac{2}{3}}\left[c_{10}\mathbf{I} + \frac{c_1}{2}e^{c_2(\overline{I_4}-1)}\mathbf{A}_0\right] \\ & - \frac{2}{3}J^{-\frac{2}{3}}\left[c_{10}\overline{I_1} + \frac{c_1}{2}e^{c_2(\overline{I_4}-1)}\overline{I_4}\right]\overline{\mathbf{C}}^{-1}.\end{aligned} \tag{41}$$

This variant of the model is also available in the ANSYS commercial software and thus facilitates a comparison of the efficiency of the algorithms. The deviatoric part of the strain energy density of the GOH model, generalized for two families of fibers, is

$$\overline{\Psi} = c_{10}\left(\overline{I_1} - 3\right) + \frac{c_1}{2c_2}\left(e^{c_2(\overline{I_4}-1)} - 1\right) + \frac{k_1}{2k_2}\left(e^{k_2(\overline{I_6}-1)} - 1\right), \tag{42}$$

and the corresponding deviatoric part of the second Piola–Kirchhoff stress is

$$\begin{aligned}\overline{\mathbf{S}} = {} & 2J^{-\frac{2}{3}}\left[c_{10}\mathbf{I} + \frac{c_1}{2}e^{c_2(\overline{I_4}-1)}\mathbf{A}_0 + \frac{k_1}{2}e^{k_2(\overline{I_6}-1)}\mathbf{B}_0\right] \\ & - \frac{2}{3}J^{-\frac{2}{3}}\left[c_{10}\overline{I_1} + \frac{c_1}{2}e^{c_2(\overline{I_4}-1)}\overline{I_4} + \frac{k_1}{2}e^{k_2(\overline{I_6}-1)}\overline{I_6}\right]\overline{\mathbf{C}}^{-1}.\end{aligned} \tag{43}$$

The final variant of the GOH model considers a dispersion factor. The deviatoric form of the strain energy density considered is

$$\overline{\Psi} = c_{10}\left(\overline{I_1} - 3\right) + \frac{c_1}{2c_2}\left(e^{c_2(\kappa I_1 + (1-3\kappa)I_4)} - 1\right), \tag{44}$$

and the corresponding deviatoric part of the second Piola–Kirchhoff stress is given to be

$$\begin{aligned}\mathbf{S} = {} & 2J^{-\frac{2}{3}}\left(c_{10} + \kappa\frac{c_1}{2}e^{c_2\left(\kappa\overline{I_1}+(1-3\kappa)\overline{I_4}-1\right)}\right)\mathbf{I} \\ & + 2J^{-\frac{2}{3}}(1-3\kappa)\frac{c_1}{2}e^{c_2\left(\kappa\overline{I_1}+(1-3\kappa)\overline{I_4}-1\right)}\mathbf{A}_0 \\ & - \frac{2}{3}J^{-\frac{2}{3}}\left[\left(c_{10} + \kappa\frac{c_1}{2}e^{c_2\left(\kappa\overline{I_1}+(1-3\kappa)\overline{I_4}-1\right)}\right)\overline{I_1}\right]\overline{\mathbf{C}}^{-1} \\ & - \frac{2}{3}J^{-\frac{2}{3}}\left[(1-3\kappa)\frac{c_1}{2}e^{c_2\left(\kappa\overline{I_1}+(1-3\kappa)\overline{I_4}-1\right)}\overline{I_4}\right]\overline{\mathbf{C}}^{-1}.\end{aligned} \tag{45}$$

Although only one family of fibers is considered, the influence of dispersion of fibers is considered in the whole range from 0 to $\frac{1}{3}$.

6 Results

This work demonstrates the application of the ANCF element formulation to model large deformation structural behaviors, particularly for biological tissue, using hyperelastic material models. Neo-Hookean and Mooney–Rivlin models are implemented using the ANCF formulation to study beam structures with rectangular and circular cross sections. A comparative study of different material models is carried out in the large deformation setting. The physical constants for the strain energy densities considered here are taken from the earlier works of Gasser et al. [11] and Shmurak et al. [41]. Results obtained from the ANCF-element-based analyses are compared with solutions obtained from analytical solutions [17,44] and numerical results obtained from standard Finite Element approach. For the FE solutions, The ANSYS commercial software application with SOLID185 and SOLID186 elements was used. The derivation of analytical expressions for the two cross-sectional cases is given in Appendix A and obtained via symbolic computation using Maple. The ANCF computations were carried out using in-house codes written in the MATLAB environment.

6.1 The elongation of a cylinder

The deformation of solid hyperelastic cylinders is the focus of this example. This scenario is commonly used in the validation of models used to model the behavior of tendons [10,19] and rubber materials [13].

In this case, a cylindrical bar with radius $R = 0.1$ m and length $L = 1$ is considered. As for the circular faces of the cylinder, one end is fixed, and normal uniaxial forces are applied at the other end. The two material models used are the neo-Hookean (with $c_{10} = 0.9$ MPa and $d = 1$ GPa) and the five-parameter Mooney–Rivlin (with $c_{10} = -0.77$ MPa, $c_{01} = 0.91$ MPa, $c_{11} = 1.03$ MPa, $c_{20} = -0.27$ MPa, $c_{02} = -0.59$ MPa, and $d = 10$ MPa).

The results obtained from the ANCF-element-based analysis are compared with commercial FE and analytical solutions. The force–elongation behavior predicted when using the neo-Hookean material model is shown in Fig. 2 and Table 1. The corresponding result, for the five-parameter Mooney–Rivlin material is presented in Fig. 3 and Table 2. The results obtained from the ANCF formulations are much closer to the analytical solution results than are the standard FE solutions.

6.2 Beams with rectangular cross section subjected to elongation

The uniaxial loading of beams of rectangular cross section is considered in this example.

As in the previous example, the beams are subjected to elongation along their largest dimension L. The beams are considered to be of width $W = 0.1$, height $H = 0.1$, and length $L = 1$. The results are presented in both tabular and graphical form to ensure that the small differences in the results are evident.

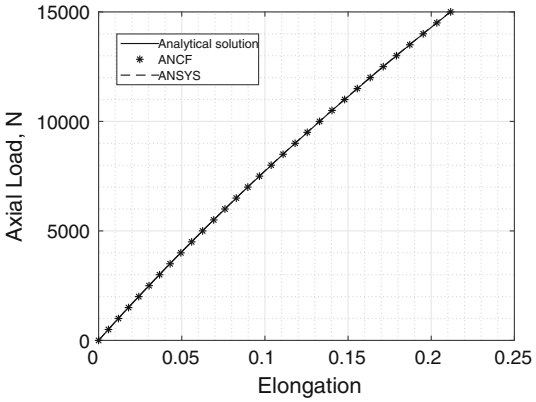

Fig. 2 Force versus elongation considering the material description by a neo-Hookean model

Table 1 Comparison of ANCF results with ANSYS and analytical solutions for material description by a neo-Hookean model

Load	Analytical	ANSYS	ANCF
500	0.00593	0.00574	0.00593
1000	0.01193	0.01171	0.01193
2000	0.02414	0.02391	0.02414
3500	0.04301	0.04278	0.04301
5000	0.06256	0.06234	0.06256
6500	0.08280	0.08260	0.08280
8000	0.10376	0.10356	0.103765
11,500	0.15558	0.15536	0.155587
13,000	0.17908	0.17884	0.179087
15,000	0.21166	0.21137	0.211665

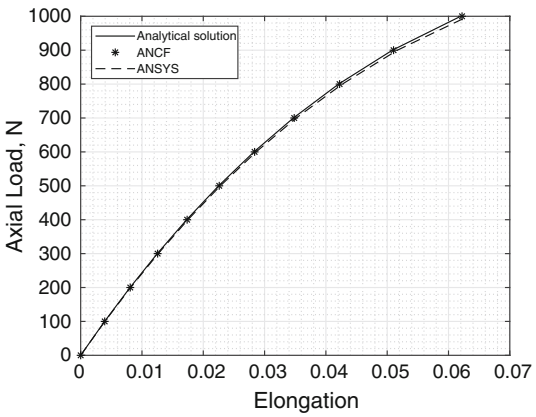

Fig. 3 Force versus elongation considering the material description by a Mooney–Rivlin model

6.2.1 Neo-Hookean material model

In the first case, the neo-Hookean material model is used to model the beam. The parameters are $c_{10} = 0.9$ MPa and $d = 1$ GPa. The comparison of results obtained between the ANCF-element-based solution and the 3D FEM solutions is shown in Fig. 4 and Table 3.

The ANCF results agree well with the analytical solution and the ANSYS solution, even when the material begins to demonstrate nonlinear behavior. The converged results of the ANCF-element-based model can be achieved with just three elements, which correspond to 36 degrees of freedom.

Table 2 Comparison of ANCF results with commercial and analytical solutions for material description by a Mooney–Rivlin model

Load	Analytical	ANSYS	ANCF
100	0.00390	0.00395	0.00392
200	0.00805	0.00815	0.00809
300	0.01250	0.01265	0.01255
400	0.01729	0.01745	0.01736
500	0.02251	0.02279	0.02260
600	0.02826	0.02862	0.02837
700	0.03469	0.03516	0.03483
800	0.04207	0.04268	0.04223
900	0.05084	0.05167	0.05104
1000	0.06198	0.06320	0.06221

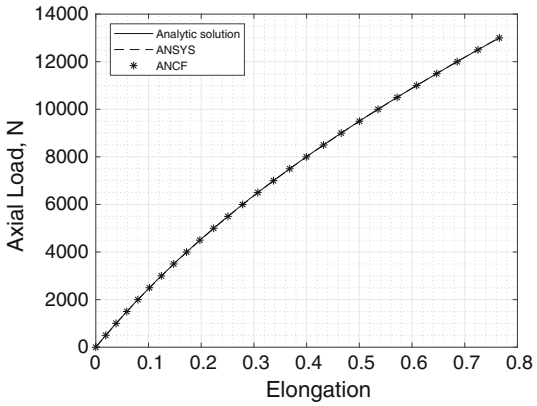

Fig. 4 Load–displacement behavior of a neo-Hookean beam subjected to uniaxial load: comparison between ANCF, 3D FEM, and analytical results for a beam of rectangular cross section

Table 3 Deformation of a neo-Hookean beam: comparison between ANCF, 3D FEM, and analytical results for a beam of rectangular cross section subjected to uniaxial load

Load	Analytical	ANSYS	ANCF
500	0.018866	0.018990	0.018869
2000	0.079830	0.080217	0.079844
3500	0.147858	0.148384	0.147887
5000	0.223538	0.224111	0.223589
8000	0.399475	0.399925	0.399594
9500	0.5	0.500297	0.500171
11,000	0.608655	0.608746	0.608894
11,500	0.646604	0.646615	0.64687
13,000	0.765329	0.765067	0.765689

6.2.2 Mooney–Rivlin material model

In this example, the two-parameter (37) and five-parameter (39) Mooney–Rivlin material models are used to model rectangular beams. For the two-parameter Mooney–Rivlin model, the parameters used are $c_{10} = 0.334$ MPa, $c_{01} = -337$ Pa, and $d = 0.1$ GPa. The deformation behaviors for this case are documented in Fig. 5 and Table 4.

Alternatively, for the five-parameter Mooney–Rivlin model, the constants considered are $c_{10} = -0.77$ MPa, $c_{01} = 0.91$ MPa, $c_{20} = -0.27$ MPa, $c_{11} = 1.03$ MPa, $c_{02} = -0.59$ MPa, and $d = 0.01$ GPa; the resulting deformation is presented in Fig. 6 and Table 5.

From the Tables, it is evident that the ANCF-element-based model results in a better approximation of the analytical deformation result, with much fewer nodes, the FE-based solution achieved by ANSYS.

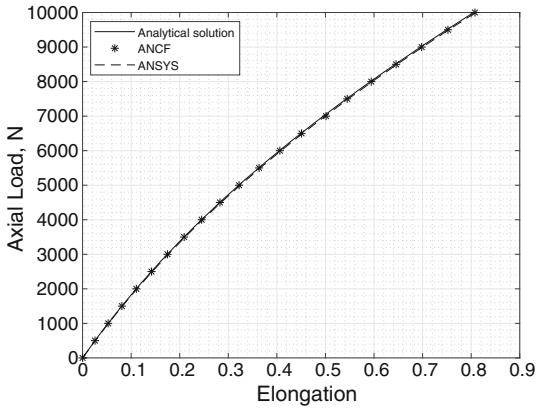

Fig. 5 Load–displacement behavior of a two-parameter Mooney–Rivlin beam: comparison between ANCF, 3D FEM, and analytical results for a beam of rectangular cross section

Table 4 Deformation of the isotropic beam of rectangular cross sections with two-constant Mooney–Rivlin model

Load	Analytical	ANSYS	ANCF
500	0.02561	0.02564	0.026018
2000	0.11053	0.11068	0.111971
5000	0.32160	0.32224	0.324556
6500	0.44961	0.45068	0.453091
8000	0.59262	0.59431	0.59649
10,000	0.80483	0.80776	0.809051

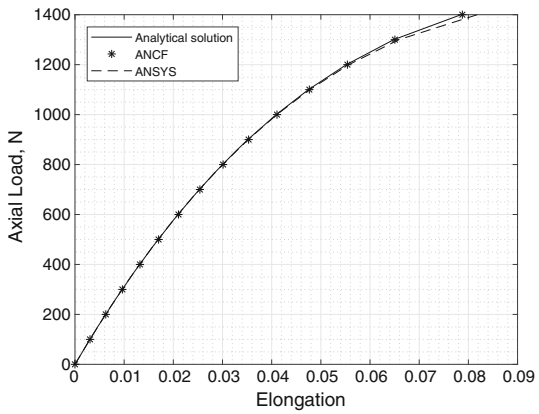

Fig. 6 Load–displacement behavior of a five-parameter Mooney–Rivlin beam: comparison between ANCF, 3D FEM, and analytical results for a beam of rectangular cross section

Table 5 Deformation of the isotropic beam of rectangular cross sections with the five constant Mooney–Rivlin model

Load	Analytical	ANSYS	ANCF
100	0.00304	0.00306	0.00304
200	0.00624	0.00627	0.00622
500	0.01693	0.01700	0.01690
1000	0.04092	0.04108	0.04106
1200	0.05520	0.05540	0.05570
1400	0.07850	0.07877	0.08181

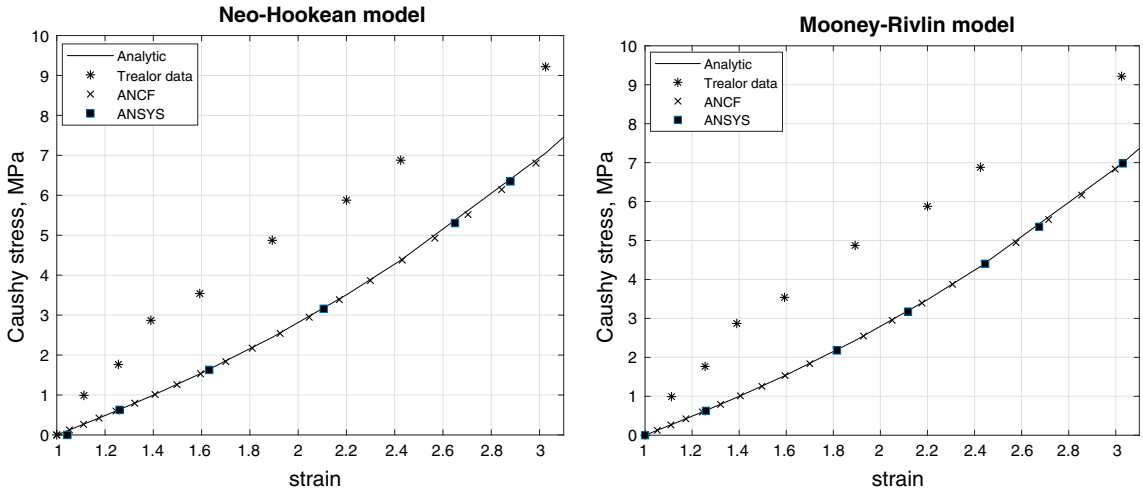

(a) Experimental, analytical, ANCF, and ANSYS stress–strain relation in tension up to 300% strain considering a Neo-Hookean material model

(b) Experimental, analytical, ANCF, and ANSYS stress–strain relation in tension up to 300% strain considering a two-constant Mooney-Rivlin material

Fig. 7 Comparison with Treloar experimental data using material parameters used in literature

6.2.3 Treloar experiments

For further validation of models based on the new ANCF elements, the classical rubber experimental data presented by in the work by Treloar [46] are reviewed here.

However, only a portion of the results is considered. The original work of Treloar presents deformation data up to 750%. In this work, the neo-Hookean and Mooney–Rivlin material models are applied. These models are only appropriate for comparison up to a maximum of 300% [32,45]. For the Treloar data, material constants for neo-Hookean (as $c_{10} = 0.4$ MPa) and two-constant Mooney–Rivlin (as $c_{10} = 0.39$ MPa and $c_{01} = 0.015$ MPa) are widely used in the literature for validation.

As shown in Fig. 7, it is evident that the constants proposed in the literature do not give accurate results in the 0–300% range. Therefore, it is necessary to propose new constants, both for the commercial FE solution and for ANCF-element-based analysis.

The recommended new set of material parameters are $c_{10} = 0.5254$ MPa for the neo-Hookean model and $c_{10} = 0.06727$ MPa and $c_{01} = 1.37485$ MPa for the Mooney–Rivlin model. The resulting force–elongation data for the new set of parameters are shown in Fig. 8a, b.

6.2.4 Anisotropic material model

In the next example, the deformation of anisotropic beams is presented. In Sect. 5, several material models were introduced, in relation to the anisotropic models. Discussed here are the results obtained via ANCF-element-based analysis using these material models. These models have been consistently used in earlier works [11,17,43]. The material parameters used in this work are taken from the work of Gasser et al. [11] and are $c_{10} = 7.64$ kPa, $c_1 = 996.6$ kPa, $c_2 = 524.6$ Pa.

The simplest, with only a single family of fibers, is first. Fiber orientation is assumed to be in the mean direction. The fiber direction, for the first case, is given as a unit vector $\boldsymbol{a}_0$ with components $\left(\frac{\sqrt{3}}{2}, 0, \frac{1}{2}\right)$. The resulting force–deformation behavior is shown in Fig. 9 and Table 6.

For the $\boldsymbol{a}_0 = \left(1/\sqrt{2}, 0, 1/\sqrt{2}\right)$ fiber direction, the resulting force–displacements are shown in Fig. 10 and Table 7.

Figures 9 and 10 show that the ANCF-based solutions offer a high degree of accuracy compared to 3D FEA, even for nonlinear cases. The convergence behavior is shown in Tables 8 and 9 for the case of the anisotropic beam with preferred orientation along $\boldsymbol{a}_0 = \left(\sqrt{3}/2, 0, 1/2\right)$. It is again evident that the ANCF formulation offers faster convergence in comparison to 3D FEA results.

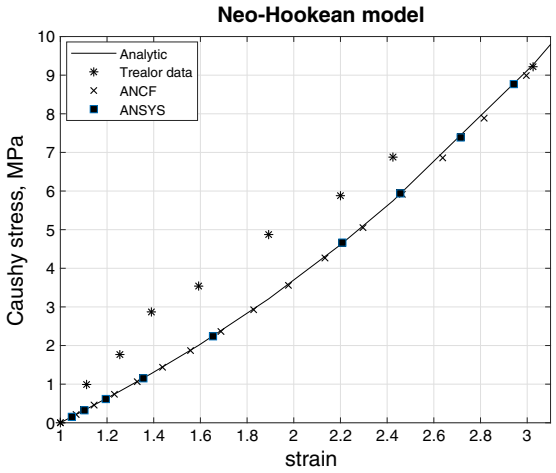

(a) Experimental, analytical, ANCF, and ANSYS stress–elongation relation considering a Neo-Hookean material model with new constants

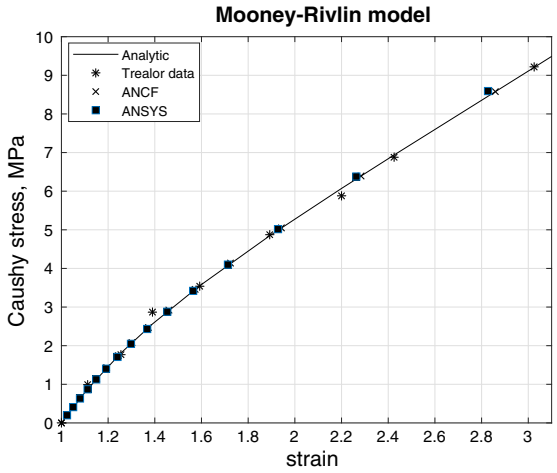

(b) Experimental, analytical, ANCF, and ANSYS stress–elongation relation considering a two-constant Mooney-Rivlin material model with new constants

Fig. 8 Comparison with Treloar experimental data using updated material parameters

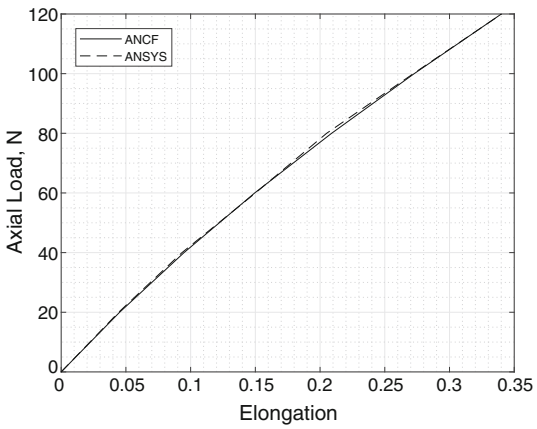

Fig. 9 Load–displacement behavior of a GOH beam: comparison between ANCF and 3D FEM results for beams of rectangular cross sections and fiber orientation along $\boldsymbol{a}_0 = \left(\sqrt{3}/2, 0, 1/2\right)$

Table 6 Load–displacement behavior of a GOH beam: comparison between ANCF and 3D FEM results for a beam of rectangular cross section and fiber orientation along $\boldsymbol{a}_0 = \left(\sqrt{3}/2, 0, 1/2\right)$

Load	ANSYS	ANCF
20	0.0444163	0.045147
40	0.0933481	0.094902
60	0.150106	0.149495
80	0.205066	0.208908
100	0.272049	0.272734
120	0.340228	0.340362

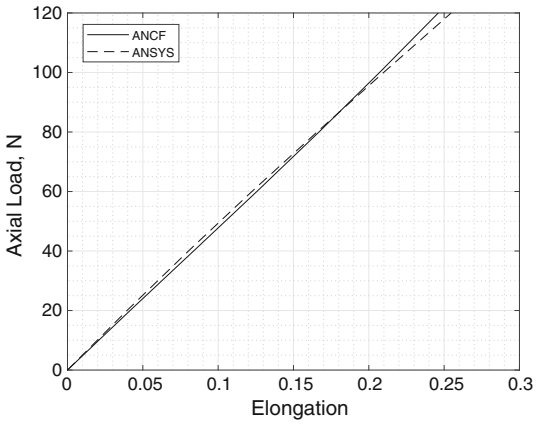

Fig. 10 Load–displacement behavior of a GOH beam: comparison between ANCF and 3D FEM results for beams of rectangular cross sections with fiber orientation along $\boldsymbol{a}_0 = \left(1/\sqrt{2}, 0, 1/\sqrt{2}\right)$

Table 7 Load–displacement behavior of a GOH beam: comparison between ANCF and 3D FEM results for a beam of rectangular cross section with fiber orientation along $\boldsymbol{a}_0 = \left(1/\sqrt{2}, 0, 1/\sqrt{2}\right)$

Load	ANSYS	ANCF
20	0.0394922	0.041532
40	0.0802718	0.083686
60	0.122392	0.125684
80	0.165644	0.166945
100	0.209808	0.207137
120	0.254683	0.246133

Table 8 Convergence behavior of ANSYS elements

DOFs	ANSYS
96	0.341577
153	0.343201
243	0.342766
1275	0.342487
14,883	0.342052
24,843	0.341553
56,355	0.340798
79,059	0.340498
92,400	0.340334
107,163	0.340228

Table 9 Convergence behavior of ANCF elements

DOFs	ANCF
27	0.340358490833798
45	0.340361806744267
81	0.340362158053474
153	0.340362204033327
297	0.340362210306283
585	0.340362211026671

6.2.5 Anisotropic material model with two families of fibers

In this example, the Eq. (42) anisotropic model is investigated. As described, the material is reinforced by two families of fibers. For the two cases considered here, the fiber directions are as follows.

1. Case 1: $\boldsymbol{a}_0 = \left(\frac{\sqrt{2}}{2}, 0, \frac{\sqrt{2}}{2}\right)$ and $\boldsymbol{b}_0 = \left(\frac{\sqrt{2}}{2}, 0, -\frac{\sqrt{2}}{2}\right)$;
2. Case 2: $\boldsymbol{a}_0 = \left(\frac{1}{2}, 0, \frac{\sqrt{3}}{2}\right)$ and $\boldsymbol{b}_0 = \left(\frac{1}{2}, 0, -\frac{\sqrt{3}}{2}\right)$.

The geometry, loading conditions, and physical constants for both examples in this Subsection are the same as and equal to those used in Sect. 6.2.4 (Figs. 11, 12).

It is evident that the obtained results, both numerical solutions—ANCF and ANSYS, are still well matched. At higher loads, the difference is about 4% at maximum load (Tables 10, 11).

6.2.6 Anisotropic beams considering the κ model

So far, anisotropic models with a particular fiber orientation have been discussed. In many biological tissues, however, fibers can change orientation or undergo disruption [19]. Therefore, it is important to represent in the model these changes. To address this scenario, the next example considers the κ model [17]. The related strain energy density for this model is as described in (44).

To evaluate the influence of the dispersion parameter κ, a single family of fibers is used as reinforcement. The dispersion parameter falls within the range $\kappa \in [0, 0.333]$. The other constants such as geometry, loading

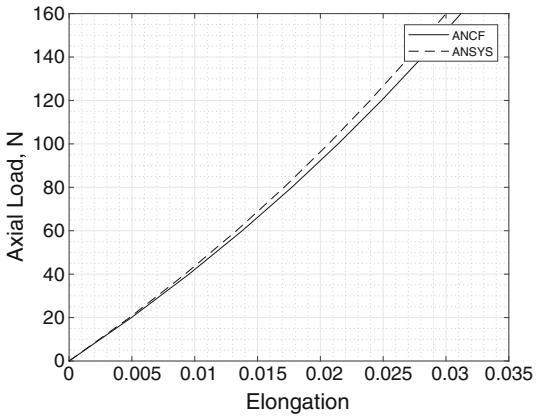

Fig. 11 Load–displacement behavior of beams with two families of fibers, namely, $\boldsymbol{a}_0 = \left(1/2, 0, \sqrt{3}/2\right), \boldsymbol{b}_0 = \left(1/2, 0, -\sqrt{3}/2\right)$

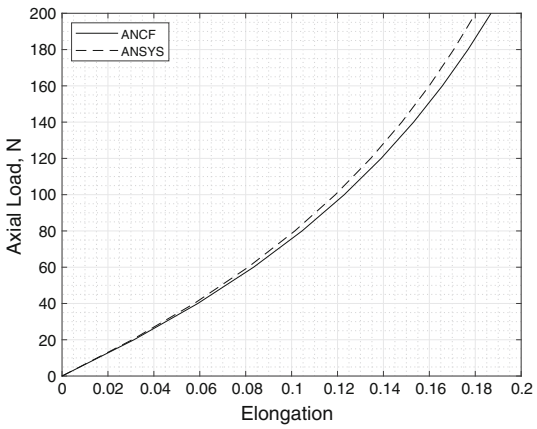

Fig. 12 Load–displacement behavior of beams with two families of fibers, namely $\boldsymbol{a}_0 = \left(1/\sqrt{2}, 0, 1/\sqrt{2}\right)$, $\boldsymbol{b}_0 = \left(1/\sqrt{2}, 0, -1/\sqrt{2}\right)$

Table 10 Load–displacement behavior of beams with two families of fibers, namely, $\boldsymbol{a}_0 = \left(1/2, 0, \sqrt{3}/2\right)$, $\boldsymbol{b}_0 = \left(1/2, 0, -\sqrt{3}/2\right)$

Load	ANCF	ANSYS
20	0.004965	0.0048108
40	0.009542	0.00923268
60	0.013782	0.0133195
80	0.017728	0.0171146
100	0.021415	0.0206535
120	0.024871	0.0239655
140	0.028122	0.0270754
160	0.031188	0.0300039
180	0.034087	0.032769
200	0.036835	0.0353859

Table 11 Load–displacement behavior of beams with two families of fibers, namely $\boldsymbol{a}_0 = \left(1/\sqrt{2}, 0, 1/\sqrt{2}\right)$, $\boldsymbol{b}_0 = \left(1/\sqrt{2}, 0, -1/\sqrt{2}\right)$

Load	ANCF	*ANSYS*
20	0.031334	0.0305561
40	0.059141	0.0575575
60	0.083443	0.0810563
80	0.104566	0.101412
100	0.122945	0.11907
120	0.139011	0.13447
140	0.153144	0.147991
160	0.165665	0.159951
180	0.176837	0.170607
200	0.186872	0.180172

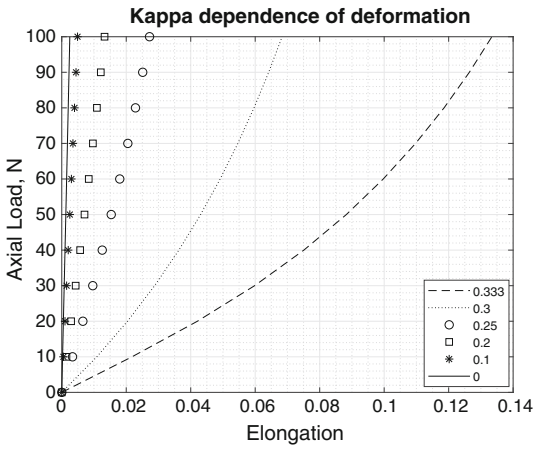

Fig. 13 Deformation of the κ model for $\mathbf{a}_0 = (1, 0, 0)$

conditions, and material parameters remain as in the previous example, i.e., $c_{10} = 7.64$ kPa, $c_1 = 996.6$ kPa, $c_2 = 524.6$ Pa with $\boldsymbol{a}_0 = \left(\frac{\sqrt{2}}{2}, 0, \frac{\sqrt{2}}{2}\right)$.

As shown in Fig. 13, the dispersion parameter significantly influences the deformation. Although the behavior is much the same in the beginning, the variation becomes significant with increased loading. The smallest elongation for this fiber direction occurs when the parameter is close to the maximum value. The larger the dispersion parameter becomes, the closer the result is to the isotropic case defined in (40).

7 Conclusions

The responses of beam-like structures using two different numerical analysis element technologies, namely the ANCF and standard FEA, are compared in this work. The ANCF framework made use of in-house codes based on MATLAB, while the FEA used the commercial finite element code ANSYS. The 3D FEA analyses were included for validation, and they served to demonstrate the computational advantage of the new ANCF-element-based beam models. The different results from the two approaches were represented in tabular and graphic forms and compared with analytical solutions.

This work compares the behavior for five hyperelastic free energy functions as a validation of the accuracy and performance of our algorithm. These include the neo-Hookean, two types of Mooney–Rivlin, and three variations of the GOH model. For the last anisotropic case, the variation in the material parameters, namely the number of fiber families and the value of the dispersion parameter is considered and demonstrated.

The obtained results demonstrate convincingly that the ANCF elements agreed, within reasonable limits, with those obtained from analytical solutions and 3D FEM. The work also demonstrates that the considered three-noded 3D ANCF element provides reasonable accuracy and good convergence behavior for modeling uniaxial modes of deformation. Furthermore, the ANCF-element-based analyses converge better than the 3D FEM analyses. The ANCF-based solutions provide good approximations to capture the nonlinear behaviors of deformation. When used to model an isotropic bar, the ANCF-element-based results better matched analytical solution results. For the GOH material cases, the ANCF and ANSYS model results both matched well within reasonable error.

In summary, the ANCF element formulation is suitable for the finite element numerical analysis of soft tissues. As demonstrated, it gives an excellent approximation of deformations, and at the same time, it requires fewer elements. As a result, it results in fewer degrees of freedom and faster convergence.

Acknowledgements We would like to thank the Research Foundation of the Lappeenranta University of Technology and the Academy of Finland (Application No. 299033 for funding 519 of Academy Research Fellow) for the generous grants that made this work possible.

Appendix A: Analytical solution

The analytical solution which we use in this paper has been outlined here. Firstly, we assume an object without any holes or different types of imperfections. Also, we assume that the material is isotropic in nature. Let us now consider the total volumes of them in the initial configuration, which can be expressed for cylindrical or rectangular bars in the forms

$$V_{\text{cyl}} = \pi L R^2,\ V_{\text{rec}} = HWL. \tag{46}$$

Upon application of load, the largest dimensions of them, i.e., let us assume it to be L, changes by λ times. If we consider the material to be incompressible, then the volume of the object does not change; from here for the cylinder, we have received $r = \frac{R}{\sqrt{\lambda}}$, and in the rectangular cross-sectional case, we have $w = \frac{W}{\sqrt{\lambda}}$, $h = \frac{H}{\sqrt{\lambda}}$, where r, h, w are dimensions of circular and rectangular cross sections in actual configurations.

The Cauchy stress tensor for the incompressible solids can be given as

$$\sigma = -p\mathbf{I} + 2\mathbf{F}\left(\frac{\partial \Psi}{\partial \mathbf{C}}\right)\mathbf{F}^T \tag{47}$$

where Ψ is potential density function, p is a function of hydrostatic stress (which is not determined by the deformation). $\mathbf{C}$ is the right Cauchy–Green tensor. However, p is not established from deformation; it is possible to receive it from boundary conditions. Our deformation occurs along one of the axes, let's name this axis z, the components of stress tensors in others, i.e., x and y are equal to zero. From this condition, the form of p is possible to derive and then substitute into σ_{zz}. The final expressions for the applied loads from which we can obtain the values of λ and as a result define the total displacements are

$$N_{\text{cyl}} = 2\pi \int_0^r \sigma_{zz} r \mathrm{d}r,\ N_{\text{rec}} = \int_0^h \int_0^w \sigma_{zz} \mathrm{d}x \mathrm{d}y. \tag{48}$$

References

1. Bauchau, O.A., Han, S., Mikkola, A., Matikainen, M.K.: Comparison of the absolute nodal coordinate and geometrically exact formulations for beams. Multibody Syst. Dyn. **32**, 67–85 (2014)
2. Bauchau, O.A., Han, S., Mikkola, A., Matikainen, M.K., Gruber, P.: Experimental validation of flexible multibody dynamics beam formulations. Multibody Syst. Dyn. **34**, 373–389 (2015)
3. Bauchau, O.A., Wu, G., Betsch, P., Cardona, A., Gerstmayr, J., Jonker, J.B., Masarati, P., Sonneville, V.: Validation of flexible multibody dynamics beam formulations using benchmark problems. Multibody Syst. Dyn. **37**, 29–48 (2016)
4. Betsch, P. (ed.): Structure-preserving integrators in nonlinear structural dynamics and flexible multibody dynamics. In: CISM International Centre for Mechanical Sciences, vol 565, 1st edn. Springer, Berlin (2016)
5. Bozorgmehri, B., Hurskainen, V.V., Matikainen, M.K., Mikkola, A.: Dynamic analysis of rotating shafts using the absolute nodal coordinate formulation. J. Sound Vib. **453**, 214–236 (2019)
6. Doll, S., Schweizerhof, K.: On the development of volumetric strain energy functions. J. Appl. Mech. **67**, 17–21 (1999)
7. Ebel, H., Matikainen, M.K., Hurskainen, V.V., Mikkola, A.: Higher-order beam elements based on the absolute nodal coordinate formulation for three-dimensional elasticity. Nonlinear Dyn. **88**, 1075–1091 (2017)
8. Escalona, J.L., Hussien, H.A., Shabana, A.A.: Application of absolute nodal co-ordinate formulation to multibody system dynamics. J. Sound Vib. **214**, 833–851 (1998)
9. Flory, P.J.: Thermodynamic relations for high elastic materials. Trans. Faraday Soc. **57**, 829–838 (1961)
10. Franchi, M., Trirè, A., Quaranta, M., Orsini, E., Ottani, V.: Collagen structure of tendon relates to function. Sci. World J. **7**, 404–420 (2007)
11. Gasser, T.C., Ogden, W.R., Holzapfel, G.A.: Hyperelastic modelling of arterial layers with distributed collagen fibre orientations. J. R. Soc. Interface **3**, 15–35 (2006)
12. Gerstmayr, J., Sugiyama, H., Mikkola, A.: Review on the absolute nodal coordinate formulation for large deformation analysis of multibody systems. J. Comput. Nonlinear Dyn. **8**, 031016 (2013)
13. Gonçalves, P.B., Pamplona, D., Lopes, S.R.X.: Finite deformations of an initially stressed cylindrical shell under internal pressure. Int. J. Mech. Sci. **5**, 92–103 (2008)
14. Grossi, E., Shabana, A.A.: Analysis of high-frequency ANCF modes: Navier-stokes physical damping and implicit numerical integration. Acta Mech. **230**, 2581–2605 (2019)
15. Holzapfel, G.: Determination of material models for arterial walls from uniaxial extension tests and histological structure. J. Theor. Biol. **238**, 290–302 (2006)
16. Holzapfel, G.A., Gasser, T.C.: A viscoelastic model for fiber-reinforced composites at finite strains: continuum basis, computational aspects and applications. Comput. Methods Appl. Mech. Eng. **190**, 4379–4403 (2001)
17. Holzapfel, G.A., Ogden, R.W.: Constitutive modelling of arteries. Proc. Math. Phys. Eng. Sci. **466**, 1551–1597 (2010)
18. Horgan, C.O., Saccomandi, G.: Constitutive modelling of rubber-like and biological materials with limiting chain extensibility. Math. Mech. Solids **7**, 353–371 (2002)
19. Khayyeri, H., Longo, G., Gustafsson, A., Isaksson, H.: Comparison of structural anisotropic soft tissue models for simulating achilles tendon tensile behaviour. J. Mech. Behav. Biomed. Mater. **61**, 431–443 (2016)
20. Kulkarni, S., Shabana, A.A.: Spatial ANCF/CRBF beam elements. Acta Mech. **230**, 929–952 (2019)
21. Li, W.: Biomechanical property and modelling of venous wall. Prog. Biophys. Mol. Biol. **133**, 56–75 (2018)
22. Lu, S.H.C., Pister, K.S.: Decomposition of deformation and representation of the free energy function for isotropic thermoelastic solids. Int. J. Solids Struct. **11**, 927–934 (1975)
23. Maqueda, L., Shabana, A.: Poisson modes and general nonlinear constitutive models in the large displacement analysis of beams. Multibody Syst. Dyn. **18**, 375–396 (2007)
24. Maqueda, L.G., Shabana, A.A.: Nonlinear constitutive models and the finite element absolute nodal coordinate formulation. In: ASME Proc. 6th International Conference on Multibody Systems, Nonlinear Dynamics, and Control, Parts A, B, and C, vol. 5, pp. 1033–1037 (2007)
25. Maqueda, L.G., Bauchau, O.A., Shabana, A.A.: Effect of the centrifugal forces on the finite element eigenvalue solution of a rotating blade: a comparative study. Multibody Syst. Dyn. **19**, 281–302 (2008)
26. Meister, T.A., Rexhaj, E., Rimoldi, S.F., Scherrer, U., Sartori, C.: Fetal programming and vascular dysfunction. Artery Res. **21**, 69–77 (2018)
27. Mikkola, A.M., Shabana, A.A.: A non-incremental finite element procedure for the analysis of large deformation of plates and shells in mechanical system applications. Multibody Syst. Dyn. **9**, 283–309 (2003)
28. Mooney, M.: A theory of large elastic deformation. J. Appl. Phys. **11**, 582–592 (1940)
29. Nachbagauer, K.: State of the art of ANCF elements regarding geometric description, interpolation strategies, definition of elastic forces, validation and the locking phenomenon in comparison with proposed beam finite element. Arch. Comput. Methods Eng. **21**, 293–319 (2014)
30. Nachbagauer, K., Pechstein, A.S., Irschik, H., Gerstmayr, J.: A new locking-free formulation for planar, shear deformable, linear and quadratic beam finite elements based on the absolute nodal coordinate formulation. Multibody Syst. Dyn. **26**(3), 245–263 (2011)
31. Nachbagauer, K., Gruber, P., Gerstmayr, J.: Structural and continuum mechanics approaches for a 3D shear deformable ANCF beam finite element: application to static and linearized dynamic examples. J. Comput. Nonlinear Dyn. **8**, 021004 (2013)
32. Nah, C., Lee, G.B., Lim, J., Kim, Y., SenGupta, R., Gent, A.: Problems in determining the elastic strain energy function for rubber. Int. J. Non-Linear Mech. **45**, 232–235 (2010)
33. Ogden, R.W.: Elastic ddformations of rubberlike solids. In: Hopkins, H.G., Sewell, M.J. (eds.) Mechanics of Solids, Mechanics of Solids: The Rodney Hill 60th Anniversary, pp. 499–537. Elsevier, Amsterdam (1982)
34. Orzechowski, G., Frączeks, J.: Nearly incompressible nonlinear material models in the large deformation analysis of beams using ANCF. Nonlinear Dyn. **82**, 451–464 (2015)

35. Patel, M., Shabana, A.A.: Locking alleviation in the large displacement analysis of beam elements: the strain split method. Acta Mech. **229**, 2923–2946 (2018)
36. Pierre, B., Stéphane, A., Susan, L., Michael, S.: Mechanical identification of hyperelastic anisotropic properties of mouse carotid arteries. In: Proulx, T. (ed.) Mechanics of Biological Systems and Materials, vol. 2, pp. 11–17. Springer, New York (2011)
37. Rachev, A., Greenwald, S.E.: Residual strains in conduit arteries. J. Biomech. **36**, 661–670 (2003)
38. Rivlin, R.S.: Large elastic deformations of isotropic materials. IV. Further developments of the general theory. Philos. Trans. R. Soc. Lond. Ser. A Math. Phys. Sci. **241**, 379–397 (1948)
39. Shabana, A.A.: Definition of the slopes and the finite element absolute nodal coordinate formulation. Multibody Syst. Dyn. **1**, 339–348 (1997)
40. Shen, Z., Li, P., Liu, C., Hu, G.: A finite element beam model including cross-section distortion in the absolute nodal coordinate formulation. Nonlinear Dyn. **77**(3), 1019–1033 (2014)
41. Shmurak, M.I., Kuchumov, A.G., Voronova, N.O.: Hyperelastic models analysis for description of soft human tissues behavior. Master's J. **1**, 230–243 (2017)
42. Simo, J.C., Taylor, R.L., Pister, K.S.: Variational and projection methods for the volume constraint in finite deformation elasto-plasticity. Comput. Methods Appl. Mech. Eng. **51**, 177–208 (1985)
43. Skarel, P., Bursa, J.: Comparison of constitutive models of arterial layers with distributed collagen fibre orientations. Acta Bioeng. Biomech. **16**, 47–58 (2014)
44. Sokhanvar, S., Dargahi, J., Packirisamy, M.: Hyperelastic modelling and parametric study of soft tissue embedded lump for mis applications. Int. J. Med. Robot. Comput. Assist. Surg. **4**, 232–241 (2008)
45. Steinmann, P., Hossain, M., Possart, G.: Hyperelastic models for rubber-like materials: consistent tangent operators and suitability for Treloar's data. Arch. Appl. Mech. **89**, 1183–1217 (2012)
46. Treloar, L.R.G.: Stress-strain data for vulcanised rubber under various types of deformation. Trans. Faraday Soc. **40**, 59–70 (1944)
47. Weiss, J.A., Gardiner, J.C.: Computational modeling of ligament mechanics. Crit. Rev. Biomed. Eng. **29**, 303–371 (2001)
48. Weiss, J.A., Maker, B.N., Govindjee, S.: Finite element implementation of incompressible, transversely isotropic hyperelasticity. Comput. Methods Appl. Mech. Eng. **135**, 107–128 (1996)